



# Template-free synthesis of porous graphitic carbon nitride microspheres for enhanced photocatalytic hydrogen generation with high stability

Quan Gu<sup>a</sup>, Yusen Liao<sup>a</sup>, Lisha Yin<sup>a</sup>, Jinlin Long<sup>b</sup>, Xuxu Wang<sup>b</sup>, Can Xue<sup>a,\*</sup>

<sup>a</sup> School of Materials Science and Engineering, Nanyang Technological University, 50 Nanyang Avenue, Singapore 639798, Singapore

<sup>b</sup> Research Institute of Photocatalysis, State Key Laboratory of Photocatalysis on Energy and Environment, Fuzhou University, Fuzhou 350002, PR China

## ARTICLE INFO

### Article history:

Received 19 August 2014

Received in revised form 8 October 2014

Accepted 16 October 2014

Available online 27 October 2014

### Keywords:

Photocatalysis

Carbon nitride

Microspheres

Solvothermal method

Hydrogen production

## ABSTRACT

Graphitic carbon nitride microsphere photocatalysts were prepared through a template-free solvothermal approach with post-heating treatment. Structural characterization results reveal that the as-prepared sample has the same composition as bulk g-C<sub>3</sub>N<sub>4</sub>, but appears as hierarchical microspheres with nanoporous surfaces. Comparing to the bulk g-C<sub>3</sub>N<sub>4</sub>, these porous microspheres exhibit narrowed bandgap and lower resistance, which allows more effective visible-light harvesting and more efficient transport and separation of photogenerated charge carriers. Consequently, we observed high rate of photocatalytic H<sub>2</sub> production and stronger photocurrent responses under visible light irradiation. Further, the long-term photocatalytic test proved high stability of the prepared nanoporous microsphere for H<sub>2</sub> generation.

© 2014 Elsevier B.V. All rights reserved.

## 1. Introduction

Graphitic carbon nitride (g-C<sub>3</sub>N<sub>4</sub>) as a metal free polymeric semiconductor has been widely used for photocatalytic H<sub>2</sub> generation because it is non-toxic, low cost, high stability and visible light active [1–7]. However, the photocatalytic efficiency of H<sub>2</sub> generation from proton reduction over polymeric carbon nitride is usually low due to (1) limited visible-light absorption; (2) low efficiency in electron-hole separation; (3) lack of surface active sites for H<sub>2</sub> evolution [8,9]. Inspired by the shape-directed functionality in nanoscale, researchers have reported a variety of photocatalysts with specific morphology and microstructure that improve sunlight harvesting and charge-carrier separation [10–12]. In particular, the hierarchical microsphere has received great attentions for high photocatalytic activity, and promoted mass and charge transport in the packed-bed flow systems [12–14]. Recently, the fabrication of g-C<sub>3</sub>N<sub>4</sub> microsphere and hollow structures has been reported by using porous silica spheres as sacrificial templates [14–16]. Nevertheless, considering the complicated process in post-removing silica templates with additional cost, it is still highly

desirable to develop a template-free method for preparing porous microspheres of graphitic carbon nitride.

So far, the major synthetic strategy of graphitic carbon nitride is still based on the higher temperature (>400 °C) annealing of molecular precursors such as melamine and urea, which is non-controllable in the product sizes and morphologies [6,17–20]. In comparison, several groups have demonstrated that the condensation of triazine precursors through solvothermal treatment could also lead to formation of graphitic carbon nitride [21–24], which provided an opportunity to control the specific morphology and microstructure of graphitic carbon nitride at relatively lower temperature.

Herein, in this work, we report template-free synthesis of hierarchical nanoporous carbon nitride microspheres through a solvothermal method. The synthetic process is illustrated in Fig. 1 with two steps: (1) solvothermal preparation of carbon nitride microsphere (CNMS) by using melamine and cyanuric chloride as precursors; (2) annealing of CNMS at 550 °C to obtain g-C<sub>3</sub>N<sub>4</sub> microsphere (CNMS-550). For comparison purposes especially in photocatalytic H<sub>2</sub> generation, Pt nanoparticles were decorated on CNMS-550 through a wetness impregnation process. The growth mechanism of the hierarchical microspheres of graphitic carbon nitride was proposed clearly through the time-dependent experiments. The as-prepared samples were characterized in detail by X-ray diffraction (XRD), scanning electron microscopy (SEM),

\* Corresponding author.

E-mail address: [cxue@ntu.edu.sg](mailto:cxue@ntu.edu.sg) (C. Xue).

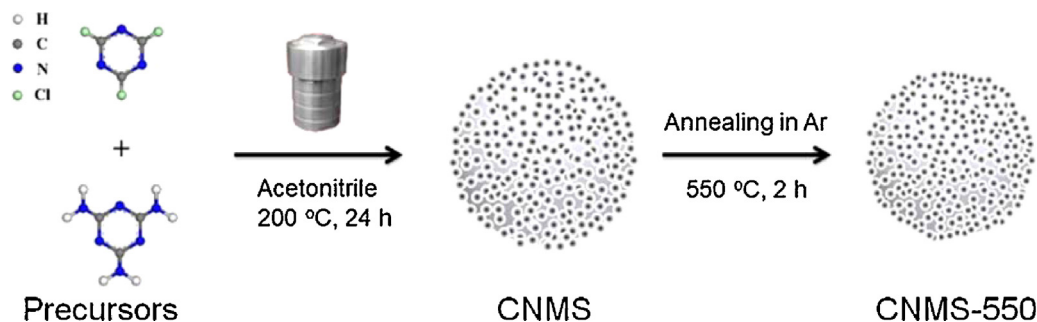


Fig. 1. Schematic illustration for the formation of g-C<sub>3</sub>N<sub>4</sub> microsphere.

transmission electron microscopy (TEM), N<sub>2</sub> physical adsorption, Fourier transform infrared spectroscopy (FTIR), X-ray photoelectron (XPS), elemental analysis, and solid-state <sup>13</sup>C nuclear magnetic resonance (NMR) spectra. Structural characterization results reveal that the as-prepared sample has the same composition as bulk g-C<sub>3</sub>N<sub>4</sub>, but appears as hierarchical microspheres with nanoporous surfaces. UV–vis spectrum, photoluminescence (PL) spectrum, and photoelectrochemical characterization were used to explore details of light adsorption and conversion, charge separation and transportation of photogenerated electrons and holes in CNMS-550. The hierarchical porous structures of obtained CNMS-550 allow for more effective visible-light harvesting and improve the transport of photogenerated charge carriers from core to surface particulates with effective suppress of radiative charge recombination and thereby enhance the photocatalytic activities.

## 2. Experimental

### 2.1. Preparation of graphitic carbon nitride microsphere (CNMS)

All chemicals used in the experiments were reagent grade and no further purification is needed before use. The CNMS was synthesis by solvothermal synthesis. Typically, 54 mg Cyanuric chloride and 18 mg melamine powders were dispersed in 60 ml acetonitrile and then mix solution was put into a 100 ml Teflon-lined autoclave. The mixture was stirred for 21 h, and then the autoclave was sealed and maintained at 200 °C for 24 h. The obtained products were sequentially washed with distilled water and absolute ethanol several. To obtain the g-C<sub>3</sub>N<sub>4</sub> like CNMS (CNMS-550), CNMS was calcined at 550 °C under the Ar flowing for 2 h.

Pt nanoparticles loaded samples (3.0 wt%) were prepared by wetness impregnation process. Typically, 40 mg of as prepared samples were first impregnated with 1.0 mg/mL H<sub>2</sub>PtCl<sub>6</sub> solutions, followed by the ultrasonic treatment for 5 min. Thereafter, the slurry was dried at 120 °C for 5 h and the obtained solid samples were further treated by NaBH<sub>4</sub> reduction. Final products were washed thoroughly with distilled water to completely remove ions and collected by centrifugation, finally dried at 120 °C.

### 2.2. Characterizations

The XRD patterns of all samples were collected on XRD-6000 X-ray diffractometer (Cu Kα source) at a scan rate of 2° min<sup>-1</sup>. SEM images were obtained by JEOL JSM-6340F scanning electron microscope set 5 kV as acceleration voltage. TEM images were obtained by a JEOL model JEM 2010 EX instrument at an accelerating voltage of 200 kV. With Lambda 750 UV/vis/NIR spectrophotometer (Perkin-Elmer, USA) using BaSO<sub>4</sub> as reference, UV–vis diffuse reflectance spectra (DRS) were measured. Fourier transform infrared spectra (FTIR) were derived from Perkin Elmer Fourier Transform Infrared Spectrometer GX. Photoluminescence

(PL) spectra were accomplished in solid with Shimadzu RF5301 Spectrofluorophotometer with an excitation wavelength of 320 nm. For photoelectrochemical experiments, the as-prepared sample was coated on fluorine-doped tin oxide (FTO) glass as the working electrode. Typically, the FTO glass with a size of 1.0 × 2.0 cm was washed in turn with acetone, ethanol, and DI water under continuous sonication, and then dried in N<sub>2</sub> flowing. By dispersing a certain amount of sample in water, the sample slurry was obtained and used for spreading onto the cleaned FTO glass substrate (photoactive area of 0.25 cm<sup>2</sup>), and dried at room temperature. Uncoated areas on the electrode were isolated with insulating tape. Photocurrent was measured by using the conventional three-electrode electrochemical cell with a working electrode, a platinum wire counter electrode and a saturated calomel electrode (SCE) as reference electrode. The working electrode was immersed in a sodium sulfate electrolyte solution (0.5 M) and irradiated by a visible light. Electrochemical impedance spectroscopy (EIS) and Mott–Schottky curves were carried out on a potentiostat Autolab PGSTAT-30 equipped with a frequency analyser module using a three-electrode system in 0.5 M Na<sub>2</sub>SO<sub>4</sub> solution.

### 2.3. Photocatalytic H<sub>2</sub> evolution

The photocatalytic hydrogen production was carried out in quartz reactor. Typically, 10 mg of the Pt loaded sample (3.0 wt%) was dispersed into 10 mL triethanolamine (TEOA, 15 vol%) aqueous solution. Before the irradiation with visible light, the suspension was degassed with N<sub>2</sub> for 15 min to remove the O<sub>2</sub> in the system. A 300 W Xenon Lamp (MAX-302, Asahi Spectra, USA) with the assistant of UV cut-off filter (λ > 420 nm) was adopted to provide the visible light. The amount of produced H<sub>2</sub> at a regular interval (1 h) was analyzed by gas chromatograph (Agilent 7890A) with TCD detector. All reactions were accomplished at room temperature. The apparent quantum efficiency (AQE) value was calculated according to the equation of  $AQE = (2 \times \text{number of evolved H}_2 \text{ molecules} / \text{number of incident photons}) \times 100\%$  [25].

## 3. Results and discussion

The XRD pattern (Fig. S1) of the obtained CNMS sample shows a clear peak at 27.3° (*d* ≈ 0.323 nm) corresponding to the (002) interlayer of graphitic carbon nitride [16,22,26], and a small peak at 17.9° attributed to one of the structural periods in the carbon-nitride layer [27,28]. The morphology and microstructure of the products are shown in Fig. 2. The low magnification SEM image (Fig. 2a) indicates that the products obtained from the solvothermal process are well-defined microspheres with an average diameter of ~2 μm. The enlarged SEM image (Fig. 2b) reveals that the products have hierarchical porous structure consisting of a microsphere core coated with nanoparticles (~10 nm diameter) and short

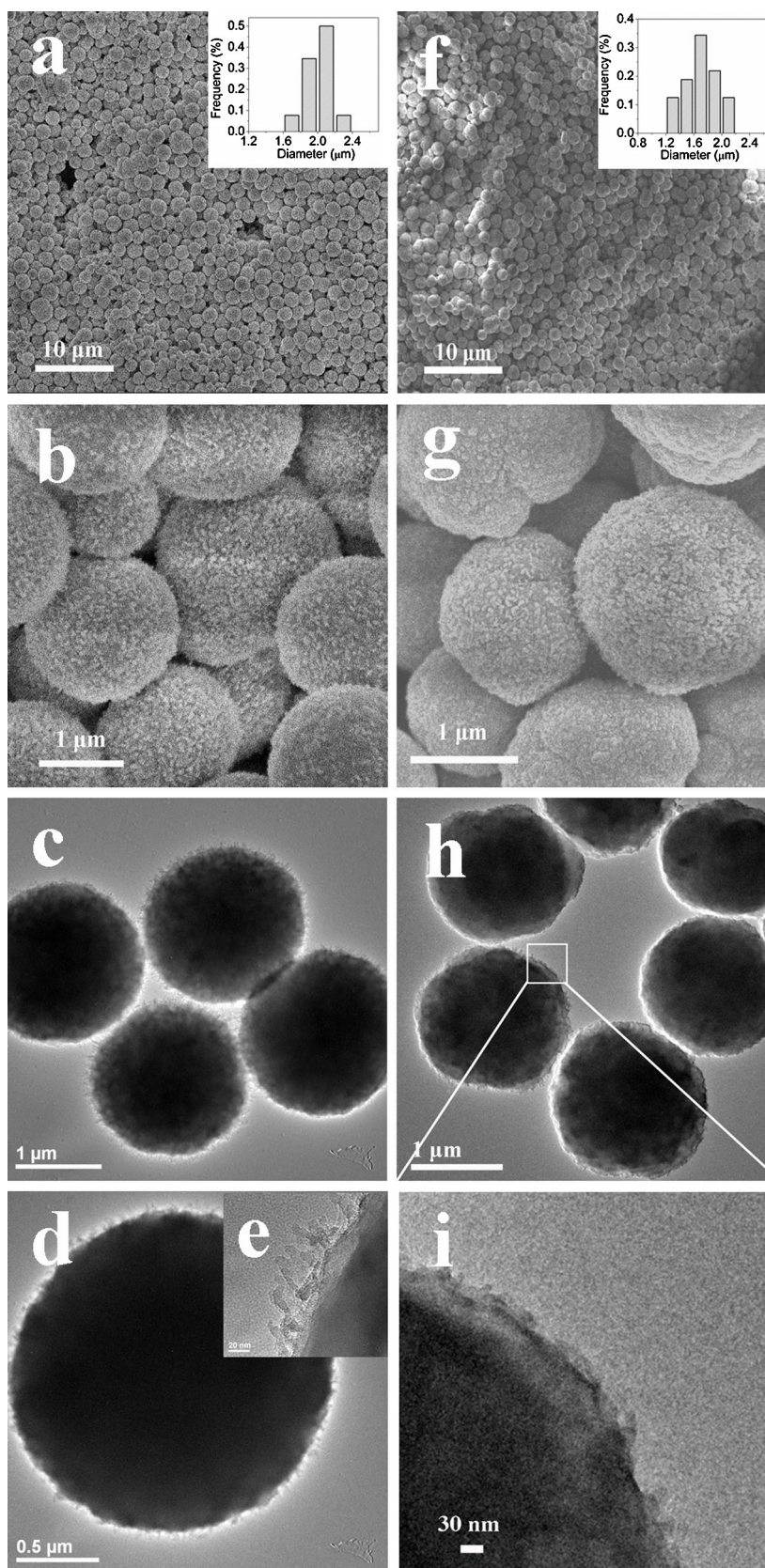


**Fig. 2.** (a) Low magnification and corresponding size distribution (inset of a), (b) high magnification SEM, (c and d) TEM images, (e) inset to (d) correspond to the enlarged areas of CNMS, (f) low magnification and corresponding size distribution (inset of f), (g) high magnification SEM, (h) TEM images, (i) correspond to the enlarged areas of CNMS-550 (h).



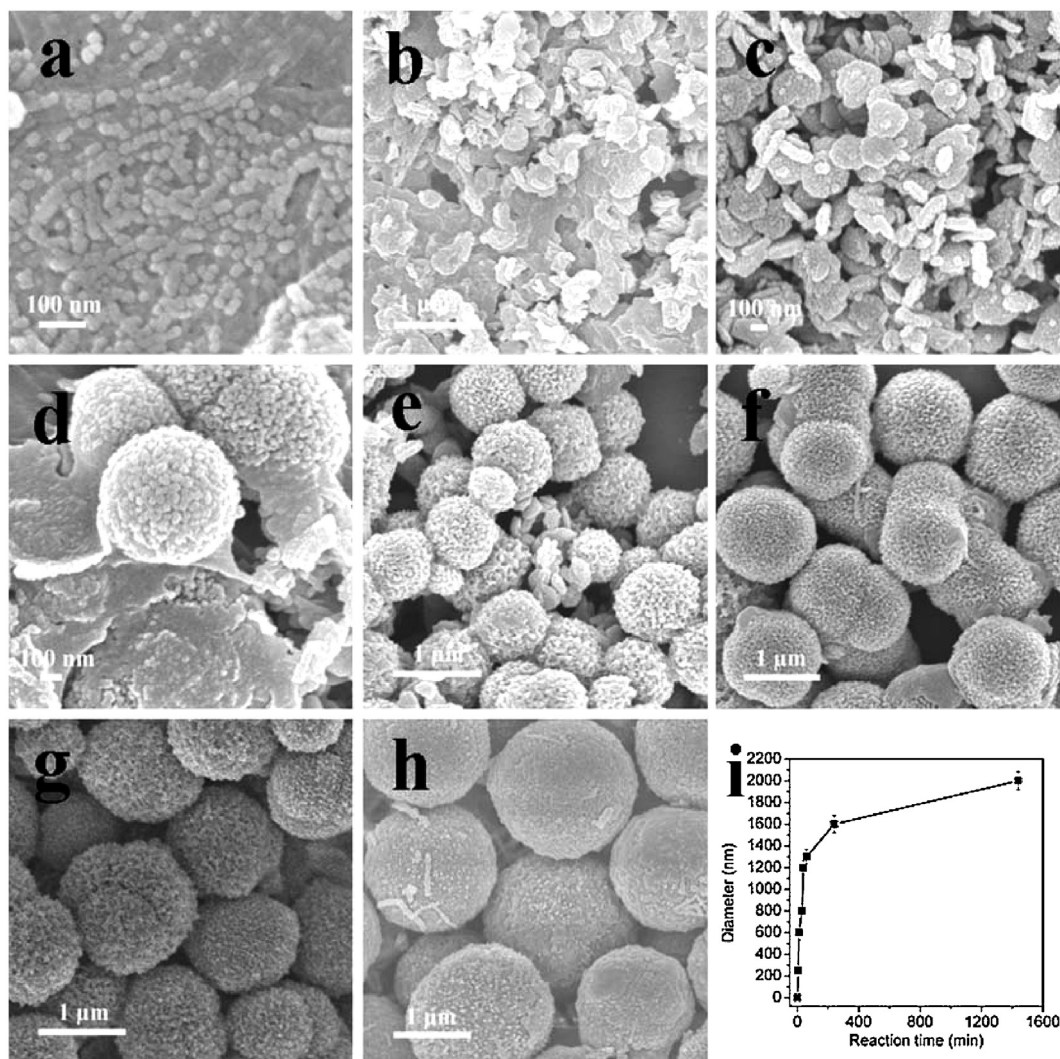


**Fig. 3.** SEM images of the prepared samples obtained at 200 °C for (a) 0 min, (b) 1 min, (c) 5 min, (d) 10 min, (e) 30 min, (f) 40 min, (g) 1 h, and (h) 24 h, respectively and (i) the relationship between the diameter of CNMS and reaction time.

nanorods (~10 nm width and 20–40 nm length), which was further confirmed by TEM images (Fig. 2c–e). After annealing at 550 °C in Ar for 2 h, the product (denoted as CNMS-550) retained microsphere morphology but with decreased diameter to around 1.7  $\mu\text{m}$  as compared between Fig. 2a and f, which indicates that heat treatment led to further re-polymerization of CNMS and subsequent size shrink. While the porous structure and small nanoparticles on the microsphere surfaces can be still observable under electron microscopic observation (Fig. 2g–i). The  $\text{N}_2$  adsorption–desorption isotherm (Fig. S2) of the hierarchical CNMS-550 sample shows the type IV shape according to the IUPAC classification [29–31], suggesting a nanoporous structure in the microsphere with pore sizes ranging from 10 to 100 nm (Fig. S2 inset).

The time-dependent experiments were carried out to explore the growth mechanism of the hierarchical microspheres. As shown in Fig. 3a, when the reaction temperature just reached 200 °C, nanoparticles with ~25 nm diameter formed on the surface of melamine particles through the condensation of cyanuric chloride and melamine [22]. With prolonged reaction time, these nanoparticles aggregated together to form irregular small sphere (Fig. 3b and c). After 10 min reaction, well-defined microspheres with diameter of ~600 nm formed through self-assembly of the nanoparticle aggregates (Fig. 3d). Further increase of reaction time led to gradual growth of CNMS with more compact structure. As shown in

Fig. 3e–h, the diameters of microspheres obtained after reaction time of 30 min, 40 min, 1 h, and 24 h are 800 nm, 1.2  $\mu\text{m}$ , 1.3  $\mu\text{m}$  and 2.0  $\mu\text{m}$ , respectively. The relationship between the diameter of CNMS and reaction time is illustrated in Fig. 3i. It indicates that in the initial stage (from 1 to 60 min), the nanoparticles aggregate via self-assembly into small spheres with rapid increase in diameter, and subsequently the formed spheres become denser with slowly increased diameter at the succeeding stages (from 1 to 24 h). This formation mechanism of the hierarchical CNMS follows is analogous to the combined processes of Oswald ripening and self-assembled aggregation, which have been reported for the growth of inorganic microspheres such as  $\text{TiO}_2$ ,  $\text{InVO}_4$ ,  $\text{NiO}$ ,  $\text{Fe}_3\text{O}_4$  and so on [29,32–35].

The effect of post-annealing of CNMS was investigated by using different characteristic techniques. For comparison, the bulk  $\text{g-C}_3\text{N}_4$  sample obtained by heating melamine was used as a reference. After annealing at 550 °C, the sample (CNMS-550) exhibits a surface area of 8.5  $\text{m}^2/\text{g}$ , which is larger than that of CNMS (5.1  $\text{m}^2/\text{g}$ ) and bulk  $\text{g-C}_3\text{N}_4$  (4.2  $\text{m}^2/\text{g}$ ). The XRD pattern of CNMS-550 (Fig. 4a) presents two diffraction peaks at 13.2° and 27.3°, which can be attributed to the in-planar packing and the (002) interlayer of a graphitic-like aromatic structure with a  $d$ -value of 0.323 nm, respectively [16,22,26,36]. This result suggests that post-annealing of CNMS led to a typical  $\text{g-C}_3\text{N}_4$  structure.

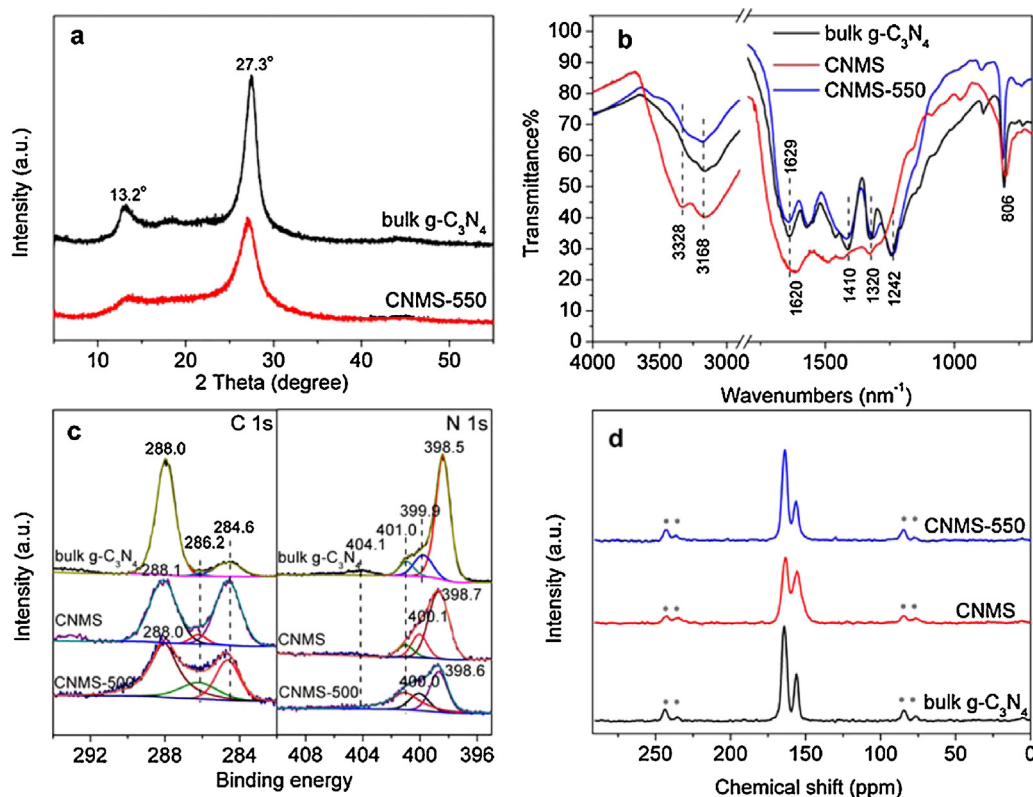


Fig. 4. (a) XRD patterns, (b) FTIR spectra, (c) XPS spectra, and (d)  $^{13}\text{C}$  CP-NMR spectra (\* shows the spinning side bands) of as prepared samples.

Fig. 4b shows the FTIR spectra of bulk  $\text{g-C}_3\text{N}_4$ , CNMS, and CNMS-550. The solvothermal product CNMS displays several characteristic bands belonging to characteristic aromatic CN heterocycles at 1620, 1410, 1320, and  $1242\text{ cm}^{-1}$ , two bands caused by the N–H stretches at  $3328$  and  $3168\text{ cm}^{-1}$ , and a band corresponding to the s-triazine ring modes at  $806\text{ cm}^{-1}$  [16,37,38]. These signals indicate condensation of cyanuric chloride and melamine occurred during solvothermal treatment. However, comparing to the FTIR spectrum of bulk  $\text{g-C}_3\text{N}_4$ , the bands at  $1620$  and  $1242\text{ cm}^{-1}$  exhibit slightly shift with lower intensity, suggesting incomplete condensation. While upon annealing at  $550^\circ\text{C}$ , the sample (CNMS-550) shows quite similar band signatures with the bulk  $\text{g-C}_3\text{N}_4$ , further indicating that the chemical structure of CNMS-550 is very close to that of bulk  $\text{g-C}_3\text{N}_4$ .

Elemental analysis was carried out to quantify the ratio of C, N, and H elements in the samples, and the results are summarized in Table S1 (see supporting information). For the CNMS sample obtained by the solvothermal process, the C/N molar ratio is about 0.69, which is slightly lower than that of bulk  $\text{g-C}_3\text{N}_4$  (0.70) prepared by heating melamine in air. This might be due to some unreacted terminal Cl elements by incomplete condensation, and consistently we did observe the Cl 2p signal in the XPS results (Fig. S3). After annealing, the C/N molar ratio of the sample (CNMS-550) increases to 0.71, which is more close to that of bulk  $\text{g-C}_3\text{N}_4$  (smaller than theoretical value of 0.75). In addition, additional small amounts of hydrogen were also identified by elemental analyses as 1.8 wt%. This might be due to the structural defects, surface termination effects by uncondensed amino functions, and adsorbed water [39–41]. It is well known that the defects can promote electron relocation in graphitic structure [39]. Thus, the sample was characterized by the electron paramagnetic resonance (EPR) to determine the structural defects. As shown in Fig S4, the EPR spectrum of CNMS-550 shows a strong signal at  $g$  value of 2.003 for the delocalized electrons in the conduction band as compared

to the bulk  $\text{g-C}_3\text{N}_4$  and CNMS [16,42], indicating that the existence of trapping states or defects on the CNMS-550 sample.

The XPS analyses results for CNMS, CNMS-550 and bulk  $\text{g-C}_3\text{N}_4$  are shown in Fig. 4c. The C 1s signals of CNMS can be fitted into three peaks centered at around 284.6, 286.2, and  $288.1\text{ eV}$ , which can be attributed to the aromatic carbon ( $\text{sp}^2\text{ C-C}$ ), the  $\text{sp}^3$  carbon at defect sites [22] and  $\text{sp}^2$ -hybridized carbon in the unit of  $\text{N-C=N}$  [4,14], respectively. The binding energy of N 1s peaks for CNMS locate at  $398.7\text{ eV}$  for  $\text{sp}^2$ -hybridized nitrogen in triazine rings ( $\text{C-N=C}$ ),  $400.1\text{ eV}$  for tertiary nitrogen  $\text{N-(C)}_3$  groups,  $401.0\text{ eV}$  for amino function ( $\text{C-N-H}$ ), and  $404.1\text{ eV}$  (the small peak) attributed to charging effects [4,14]. It is found that the binding energies of N 1s peaks for  $\text{sp}^2$ -hybridized nitrogen in triazine rings ( $\text{C-N=C}$ ) and tertiary nitrogen  $\text{N-(C)}_3$  groups of the CNMS sample increase simultaneously by  $0.2\text{ eV}$  and binding energy of C 1s for  $\text{sp}^2$ -hybridized carbon in the unit of  $\text{N-C=N}$  of the CNMS sample increases by  $0.1\text{ eV}$  as compared to the bulk  $\text{g-C}_3\text{N}_4$ . These shifts might be attributed to the high electronegative residual Cl groups on the CNMS surface, as proved by the observed Cl 2p in Fig. S3. While after annealing at  $550^\circ\text{C}$ , the Cl signal disappeared. As such, for CNMS-550, the C 1s and N 1s peaks shifted to the lower binding energy and are very close to those of bulk  $\text{g-C}_3\text{N}_4$  due to the complete removal of residual Cl upon annealing. According to these results, we can conclude that the CNMS and CNMS-550 have aromatic CN framework composed of heptazine repeating units.

The solid-state  $^{13}\text{C}$  NMR spectra of the samples are shown in Fig. 4d. The spectra of CNMS and CNMS-550 show two distinct signals at 164.2 and  $156.1\text{ ppm}$  that can be assigned to the C atoms in  $\text{CN}_2(\text{NH}_2)$  and melem ( $\text{CN}_3$ ), respectively. The result is in good agreement with those of bulk  $\text{g-C}_3\text{N}_4$  as reported by others [16,22], suggesting characteristic poly(tri-s-triazine) structures in the prepared samples. In short summary, according to the results obtained from XRD, FTIR, elemental analysis, XPS, and  $^{13}\text{C}$  NMR, we can conclude that the prepared CNMS-550 through the template-free

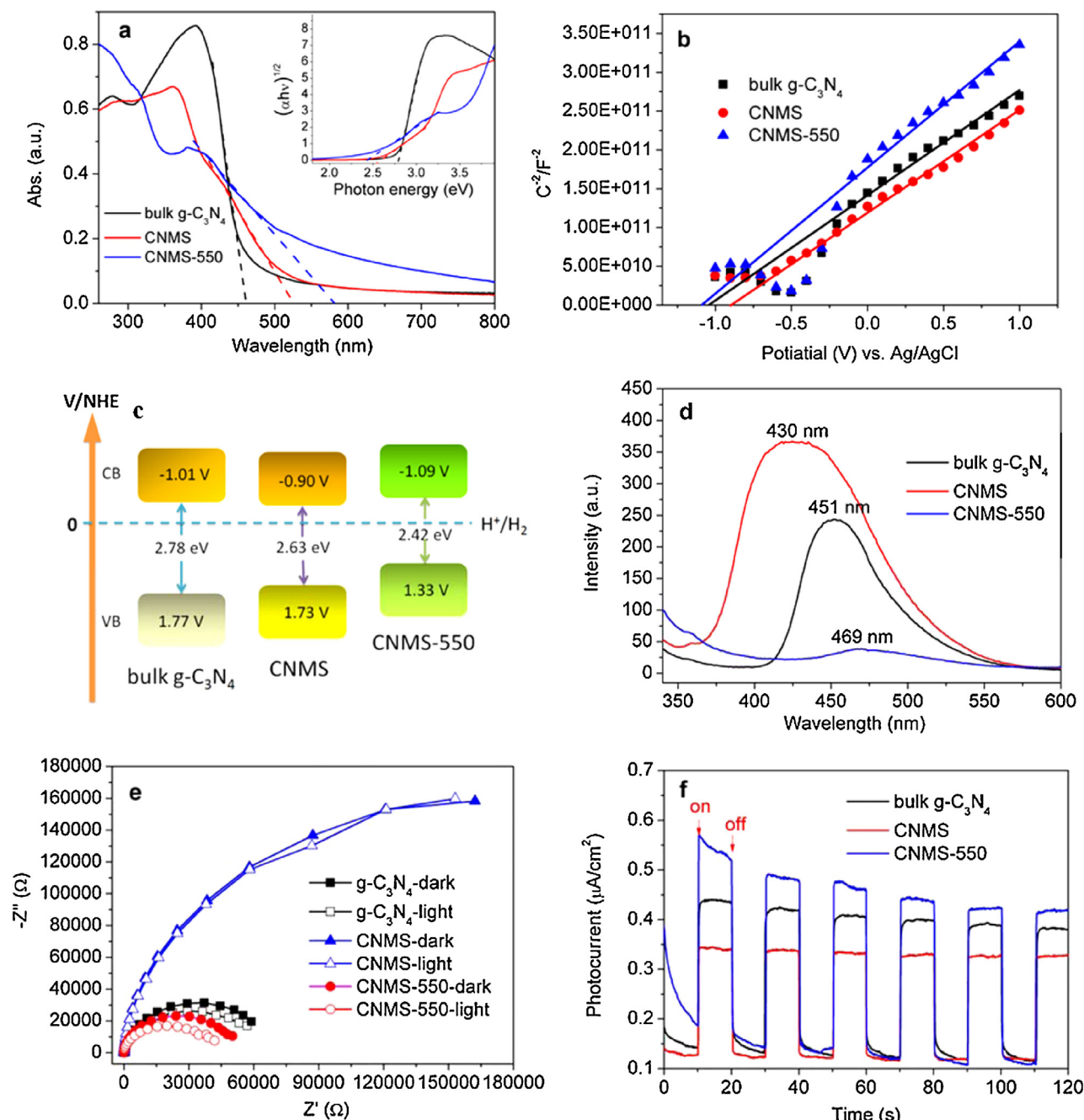


**Fig. 5.** (a) UV-vis adsorption spectra, (b) Mott-Schottky plots, (c) schematic band structure, (d) room-temperature photoluminescence spectra, (e) electrochemical impedance spectra (EIS) and (f) photocurrent under visible light in pH 7.0  $\text{Na}_2\text{SO}_4$  solution of bulk  $g\text{-C}_3\text{N}_4$ , CNMS, and CNMS-550.

solvothermal method have very similar chemical structures with regular bulk  $g\text{-C}_3\text{N}_4$ .

Fig. 5a shows the optical absorption spectra of bulk  $g\text{-C}_3\text{N}_4$ , CNMS, and CNMS-550 samples. The CNMS sample exhibits an absorption edge at 520 nm, which is longer than that of bulk  $g\text{-C}_3\text{N}_4$  (450 nm). Heating the CNMS at 550 °C under Ar flowing for 2 h resulted in a red-shifted absorption edge to 580 nm and tailed absorption in the region of 600–800 nm. The former might be due to the high degree of condensation and packing between the layers [4,36,43,44], and the latter can be attributed to trapping states or defects, which can be confirmed by PL results. According to the absorption spectra, the band gap of bulk  $g\text{-C}_3\text{N}_4$ , CNMS, and CNMS-550 obtained from UV-vis spectra are estimated as 2.78, 2.68, and 2.42 eV, respectively. By using the Mott-Schottky curves

shown in Fig. 5b, the flat-band potentials of bulk  $g\text{-C}_3\text{N}_4$ , CNMS, and CNMS-550 are identified as -1.01, -0.90, and -1.09 V, respectively. Accordingly, the band structures of bulk  $g\text{-C}_3\text{N}_4$ , CNMS, and CNMS-550 samples can be depicted as Fig. 5c.

The photoluminescence (PL) spectra of the samples were tested at an excitation wavelength of 320 nm. As shown in Fig. 5d, the CNMS shows a very strong emission peaks centered at 430 nm, which red-shifted to 469 nm upon further repolymerization by calcination at 550 °C [45]. This is consistent with the red-shift of absorption band edge after calcination, and might be due to the high degree of condensation and packing between the layers [4,36,43,44]. It is worth noting that the PL intensity of CNMS-550 is the lowest among all the samples compared to that of bulk  $g\text{-C}_3\text{N}_4$  and CNMS, due to strong non-radiative transition



by the trapping states or defects (including edges, curvature, surface C or N vacancies, and surface termination effects by uncondensed amino functions and adsorbed water) [39–41], suggesting that the radiative charge recombination is effectively inhibited by the hierarchical porous structure of CNMS-550 [14]. In addition, the electrochemical impedance spectra (Fig. 5e) indicate that the CNMS-550 has lower resistance in electron transport, and moreover, visible light irradiation led to decreased resistance with magnitude in order of CNMS < bulk  $g\text{-C}_3\text{N}_4$  < CNMS-550. Consistently, the CNMS-550 exhibited higher photocurrent responses than the CNMS and bulk  $g\text{-C}_3\text{N}_4$  (Fig. 5f). These results imply that the hierarchical porous structures of CNMS-550 improve the transport of photogenerated charge carriers from core to surface particulates with effective suppress of radiative charge recombination [28,46] and thereby enhance the photocatalytic activities.

To further verify the photocatalytic activities, the  $\text{H}_2$  generation reaction was carried out in aqueous solution with TEOA (15 vol%) as the sacrificial agent under visible light (>420 nm) and solar light irradiation, respectively. Prior to the photocatalytic test, all samples were loaded with Pt (3.0 wt%) nanoparticles by using a wetness impregnation method (the TEM of Pt loaded CNMS-550 is shown in Fig. S5, see supporting information). As shown in Fig. 6a, the CNMS showed very low  $\text{H}_2$  generation rate ( $0.016 \mu\text{mol h}^{-1}$ ) under visible light irradiation. In comparison, the post-annealed sample CNMS-550 exhibited significantly enhanced  $\text{H}_2$  generation rate ( $1.80 \mu\text{mol h}^{-1}$ , AQE is estimated as 1.62% at 420 nm), which is even 2.3 times higher than that ( $0.784 \mu\text{mol h}^{-1}$ , AQE is estimated as 0.75% at 420 nm) over the bulk  $g\text{-C}_3\text{N}_4$  and comparable to the literature result [47]. Similar trend was also observed under solar light irradiation (Fig. S6, see supporting information). In addition, the stability of CNMS-550 photocatalyst was also evaluated by recycling the reaction under the same conditions. As shown in Fig. 6b, the  $\text{H}_2$  generation rate remains constant after five times re-cycling (over 25 h). And the sample after re-cycling test still shows the same features in XRD and TEM characterizations with almost no change (Fig. S7). This indicates that the CNMS-550 photocatalyst has very good stability during the photocatalytic reaction. Moreover, we have also performed wavelength-dependent  $\text{H}_2$  evolution for 3 wt% Pt loaded CNMS-550 samples as shown in Fig. 7. The result indicated that the irradiation of light with wavelength in the range of 360–500 nm leads to the production of light-excitation electrons in the CNMS-550 and thus can drive the  $\text{H}_2$  evolution. The trend of  $\text{H}_2$  evolution is mainly concordant with the absorption spectrum of 3 wt% Pt/CNMS-550 in the range of 360–600 nm, but the conversion of absorbed light to  $\text{H}_2$  evolution is lower when the wavelength of light larger than 450 nm. In spite of this, as prepared CNMS-550 show the more effective visible-light harvesting and conversion (the effective visible light absorption threshold is evaluated to be 520 nm according to the wavelength-dependent  $\text{H}_2$  evolution).

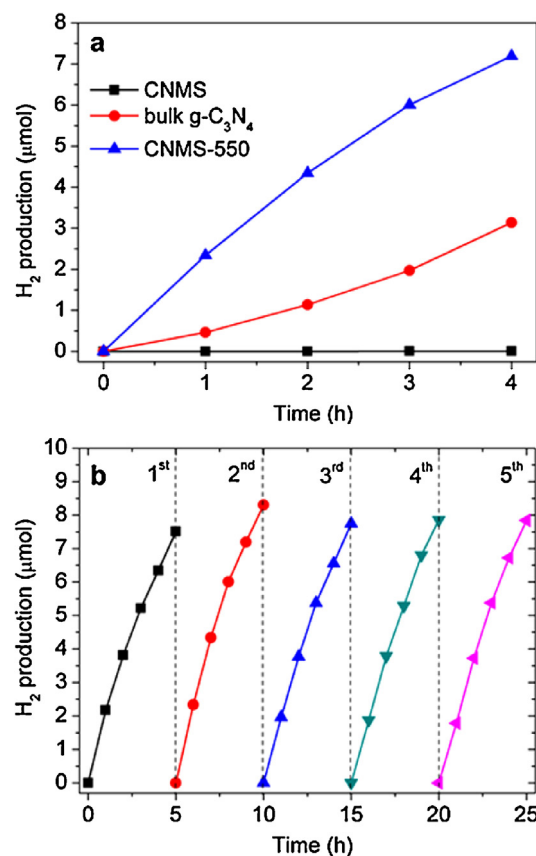


**Fig. 6.** (a) Photocatalytic hydrogen evolution under visible light irradiation (>420 nm) over bulk  $g\text{-C}_3\text{N}_4$ , CNMS, and CNMS-550 samples. (b) Stability of CNMS-550 during prolonged photocatalytic reaction.

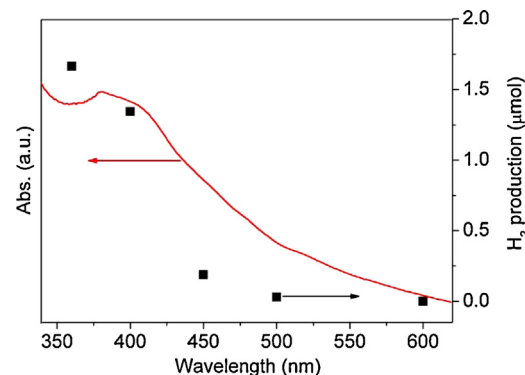
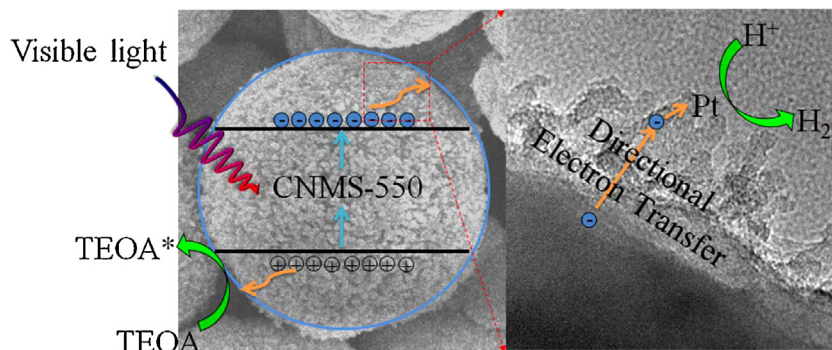


**Fig. 7.** Wavelength-dependent  $\text{H}_2$  evolution rates over as prepared graphitic carbon nitride microsphere.



**Scheme 1.** The proposed mechanism of photocatalytic hydrogen generation over the Pt loaded CNMS-550 sample.

The CNMS-550 shows higher photocatalytic activity than the other two samples for two major reasons. First, it exhibits smaller bandgap as indicated by the UV–vis spectrum (Fig. 5a), which allows more effective visible-light harvesting. Second, it has lower resistance for more efficient charge transport as proved by the measurement of transient photocurrent response and the electrochemical impedance spectroscopy (EIS) (Fig. 5e and f), which allows more effective separation of photogenerated charge carriers. Therefore, both the hierarchical porous structure and high-degree condensation play important roles for improving the photocatalytic activity. In particular, for CNMS-550, the sesame-like surface  $g\text{-C}_3\text{N}_4$  particles create homojunctions, resulting in directional transfer of photogenerated charge carriers from core to surfaces and suppress of their recombination [28,46]. The photocatalytic mechanism during hydrogen generation over the Pt loaded CNMS-550 is illustrated in Scheme 1. As such, the photocatalytic activity for  $\text{H}_2$  generation can be greatly enhanced.

#### 4. Conclusions

In summary, we have successfully prepared the hierarchical nanoporous microspheres of graphitic carbon nitride for the first time via template-free solvothermal treatment with post-annealing under Ar flowing. Comparing to the bulk  $g\text{-C}_3\text{N}_4$ , the prepared nanoporous microspheres exhibit wider-range visible light absorption and enable more effective transport and separation of photogenerated charge carrier, and thereby showed greatly enhanced photocatalytic  $\text{H}_2$  generation rate. This work provides a guide to preparing the hierarchical structure of metal free catalyst with enhanced and stable photocatalytic activity through a template-free method.

#### Acknowledgements

This work is financially supported by NTU seed funding for Solar Fuels Laboratory, MOE AcRF-Tier1 (RG 44/11), MOE AcRF-Tier2 (MOE2012-T2-2-041, ARC 5/13), and CRP (NRF-CRP5-2009-04) from NRF Singapore.

#### Appendix A. Supplementary data

Supplementary data associated with this article can be found, in the online version, at <http://dx.doi.org/10.1016/j.apcatb.2014.10.045>.

#### References

- [1] P. Niu, L. Zhang, G. Liu, H. Chen, *Adv. Funct. Mater.* 22 (2012) 4763–4770.
- [2] K. Schwinghammer, M. Mesch, V. Duppel, C. Ziegler, J. Senker, B. Lotsch, *J. Am. Chem. Soc.* 136 (2014) 1730–1733.
- [3] K. Schwinghammer, B. Tuffy, M. Mesch, E. Wirnhier, C. Martineau, F. Taulelle, W. Schnick, J. Senker, B. Lotsch, *Angew. Chem. Int. Ed.* 52 (2013) 2435–2439.
- [4] Y. Yuan, S. Cao, Y. Liao, L. Yin, C. Xue, *Appl. Catal. B: Environ.* 140 (2013) 164–168.
- [5] X. Wang, K. Maeda, X. Chen, K. Takanebe, K. Domen, Y. Hou, X. Fu, M. Antonietti, *J. Am. Chem. Soc.* 131 (2009) 1680–1681.
- [6] X. Wang, K. Maeda, A. Thomas, K. Takanebe, G. Xin, J. Carlsson, K. Domen, M. Antonietti, *Nat. Mater.* 8 (2009) 76–80.
- [7] Y. Zhao, Z. Liu, W. Chu, L. Song, Z. Zhang, D. Yu, Y. Tian, S. Xie, L. Sun, *Adv. Mater.* 20 (2008) 1777–1781.
- [8] X. Chen, S. Shen, L. Guo, S. Mao, *Chem. Rev.* 110 (2010) 6503–6570.
- [9] A. Kudo, Y. Miseki, *Chem. Soc. Rev.* 38 (2009) 253–278.
- [10] C. King'ondo, A. Iyer, E. Njagi, N. Opembe, H. Genuino, H. Huang, R. Ristau, S. Suib, *J. Am. Chem. Soc.* 133 (2011) 4186–4189.
- [11] A. Kubacka, M. Fernández-García, G. Colón, *Chem. Rev.* 112 (2011) 1555–1614.
- [12] H. Li, Z. Bian, J. Zhu, D. Zhang, G. Li, Y. Huo, H. Li, Y. Lu, *J. Am. Chem. Soc.* 129 (2007) 8406–8407.
- [13] B. Liu, L. Liu, X. Lang, H. Wang, X. Lou, E. Aydi, *Energy Environ. Sci.* (2014), <http://dx.doi.org/10.1039/c4ee00472h>.
- [14] J. Zhang, M. Zhang, C. Yang, X. Wang, *Adv. Mater.* 26 (2014) 4121–4126.
- [15] M. Groenewolt, M. Antonietti, *Adv. Mater.* 17 (2005) 1789–1792.
- [16] J. Sun, J. Zhang, M. Zhang, M. Antonietti, X. Fu, X. Wang, *Nat. Commun.* 3 (2012) 1139, <http://dx.doi.org/10.1038/ncomms2152>.
- [17] S. Cao, Y. Yuan, J. Fang, M. Shahjamali, F. Boey, J. Barber, S. Joachim Loo, C. Xue, *Int. J. Hydrogen Energy* 38 (2013) 1258–1266.
- [18] L. Yin, Y. Yuan, S. Cao, Z. Zhang, C. Xue, *RSC Adv.* 4 (2014) 6127–6132.
- [19] S. Cao, X. Liu, Y. Yuan, Z. Zhang, J. Fang, S. Loo, J. Barber, T. Sum, C. Xue, *Phys. Chem. Chem. Phys.* 15 (2013) 18363–18366.
- [20] S. Cao, X. Liu, Y. Yuan, Z. Zhang, Y. Liao, J. Fang, S. Loo, T. Sum, C. Xue, *Appl. Catal. B: Environ.* 147 (2014) 940–946.
- [21] C. Cao, F. Huang, C. Cao, J. Li, H. Zhu, *Chem. Mater.* 16 (2004) 5213–5215.
- [22] Y. Cui, Z. Ding, X. Fu, X. Wang, *Angew. Chem. Int. Ed.* 51 (2012) 11814–11818.
- [23] G. Goglio, D. Foy, G. Demazeau, *Mater. Sci. Eng. R* 58 (2008) 195–227.
- [24] X. Lu, L. Gai, D. Cui, Q. Wang, X. Zhao, X. Tao, *Mater. Lett.* 61 (2007) 4255–4258.
- [25] M. Liu, D. Jing, Zh. Zhou, L. Guo, *Nat. Commun.* 4 (2013) 2278, <http://dx.doi.org/10.1038/ncomms3278>.
- [26] X. Wang, X. Chen, A. Thomas, X. Fu, M. Antonietti, *Adv. Mater.* 21 (2009) 1609–1612.
- [27] T. Sano, S. Tsutsui, K. Koike, T. Hirakawa, Y. Teramoto, N. Negishi, K. Takeuchi, *J. Mater. Chem. A* 1 (2013) 6489–6496.
- [28] F. Dong, Z. Zhao, T. Xiong, Z. Ni, W. Zhang, Y. Sun, W. Ho, *ACS Appl. Mater. Int.* 5 (2013) 11392–11401.
- [29] Y. Li, M. Cao, L. Feng, *Langmuir* 25 (2009) 1705–1712.
- [30] F. Lu, W. Cai, Y. Zhang, *Adv. Funct. Mater.* 18 (2008) 1047–1056.
- [31] Y. Li, J. Liu, X. Huang, G. Li, *Cryst. Growth Des.* 7 (2007) 1350–1355.
- [32] C. Yuan, X. Zhang, L. Su, B. Gao, L. Shen, *J. Mater. Chem.* 19 (2009) 5772–5777.
- [33] B. Jia, L. Gao, *J. Phys. Chem. C* 112 (2007) 666–671.
- [34] H. Yang, H. Zeng, *J. Phys. Chem. B* 108 (2004) 3492–3495.
- [35] B. Liu, H. Zeng, *Small* 1 (2005) 566–571.
- [36] S. Yan, Z. Li, Z. Zou, *Langmuir* 25 (2009) 10397–10401.
- [37] B. Lotsch, M. Döblinger, J. Sehnert, L. Seyfarth, J. Senker, O. Oeckler, W. Schnick, *Chem. Eur. J.* 13 (2007) 4969–4980.
- [38] M. Bojdys, J. Müller, M. Antonietti, A. Thomas, *Chem. Eur. J.* 14 (2008) 8177–8182.
- [39] F. Goettmann, A. Fischer, M. Antonietti, A. Thomas, *Angew. Chem. Int. Ed.* 45 (2006) 4467–4471.
- [40] T. Enoki, Y. Kobayashi, *J. Mater. Chem.* 15 (2005) 3999–4002.
- [41] S. Tomita, T. Sakurai, H. Ohta, M. Fujii, S. Hayashi, *J. Chem. Phys.* 114 (2001) 7477–7482.
- [42] M. Tabbal, T. Christidis, S. Isber, P. Mérel, M.A. El Khakani, M. Chaker, A. Amasian, L. Martinu, *J. Appl. Phys.* 98 (2005) 044310–044318.
- [43] Y. Wang, X. Wang, M. Antonietti, *Angew. Chem. Int. Ed.* 51 (2012) 68–89.
- [44] B. Jürgens, E. Irran, J. Senker, P. Kroll, H. Müller, W. Schnick, *J. Am. Chem. Soc.* 125 (2003) 10288–10300.
- [45] J. Wang, D. Miller, E. Gillan, *Chem. Commun.* (2002) 2258–2259.
- [46] J. Zhang, M. Zhang, R. Sun, X. Wang, *Angew. Chem. Int. Ed.* 124 (2012) 10292–10296.
- [47] J. Chen, S. Shen, P. Guo, P. Wu, L. Guo, *J. Mater. Chem. A* 2 (2014) 4605–4612.